Quantification of anthropogenic and marine sources to atmospheric mercury over the marginal seas of China and impact assessment on 2 the sea-air exchange of mercury 3 4 Xiaofei Qin¹, Hao Li², Jia Chen³, Junjie Wei^{4,5}, Hao Ding^{4,5}, Xiaohao Wang³, Guochen Wang², 5 6 Chengfeng Liu², Da Lu², Shengqian Zhou², Haowen Li², Yucheng Zhu², Ziwei Liu², Qingyan Fu⁶, 7 Juntao Huo³, Yanfen Lin³, Congrui Deng², Yisheng Zhang^{1*}, Kan Huang^{2, 7, 8,9*} 8 9 ¹School of Environmental and Municipal Engineering, Qingdao University of Technology, Qingdao, 10 China 11 ²Shanghai Key Laboratory of Atmospheric Particle Pollution and Prevention (LAP³), National 12 Observations and Research Station for Wetland Ecosystems of the Yangtze Estuary, Department of 13 Environmental Science and Engineering, Fudan University, Shanghai, China ³Shanghai Environment Monitoring Center, Shanghai, China 14 15 ⁴Key Laboratory of Environmental Pollution Control Technology of Zhejiang Province, Hangzhou, 16 Zhejiang, China 17 ⁵Environmental Science Research & Design Institute of Zhejiang Province, Hangzhou, Zhejiang, 18 19 ⁶Shanghai Academy of Environmental Sciences, Shanghai, China 20 ⁷Institute of Eco-Chongming, Shanghai, China 21 ⁸IRDR ICoE on Risk Interconnectivity and Governance on Weather/Climate Extremes Impact and 22 Public Health, Fudan University, Shanghai, China 23 ⁹Observation and Research Station of Huaniaoshan East China Sea Ocean-Atmosphere Integrated 24 Ecosystem, Ministry of Natural Resources, Shanghai, China 25 Correspondence: huangkan@fudan.edu.cn (Kan Huang); doctorzys@163.com (Yisheng Zhang) 26

1

27

28

Abstract

Mercury in the atmosphere is a crucial environmental concern due to its toxicity and ability to travel

long distances. In the marginal seas, the contributions of terrestrial anthropogenic vs. natural sources on atmospheric mercury have been rarely quantified and their roles in mercury sea-air exchange are not well understood. To address this issue, this study integrated observations from island, cruise, and inland campaigns. The mean concentrations of TGM were 2.32 ± 1.02 ng/m³ (Bohai Sea), 2.55 \pm 0.55 ng/m³ (Yellow Sea), and 2.31 \pm 0.81 ng/m³ (East China Sea), respectively, with coastal regions exhibiting significantly higher values than open ocean areas due to continental outflows. Positive correlations were observed between total gaseous mercury (TGM) concentrations and environmental parameters such as temperature, relative humidity, and wind speed, indicating the significant influence of natural sources on atmospheric mercury in the marine environment. The application of the TGM/BC (black carbon) ratio underscored the effects of continental outflows. By utilizing a receptor model and linear regression analysis, a robust method was developed to quantitatively estimate the contribution of anthropogenic and natural sources to TGM. Anthropogenic sources accounted for an average of 59%, 3840%, and 2629% of TGM over the Bohai Sea, Yellow Sea, and East China Sea, respectively. The sea-air exchange fluxes of mercury were estimated as 0.17±0.38, 1.10±1.34, and 3.44±3.24 ng m⁻² h⁻¹ over the three seas above, respectively. To assess the potential impact of anthropogenic emissions on the sea-air exchange fluxes of mercury, After omitting anthropogenic contributions to TGM were artificially removed, then thesea-air fluxes would be increased by 207.1% in the Bohai Sea, 33.4% in the Yellow Sea, and 6.5% in the East China Sea, respectively. Upon omitting the contributions of anthropogenic sources, the sea air exchange fluxes of mercury could be enhanced by 207.1%, 32.4%, and 5.8%, respectively. This study elucidated the role of anthropogenic emissions in shaping the marine atmospheric mercury and the modulation of sea-air exchange fluxes, thereby informing valuable assessments regarding the influence of future reduced anthropogenic mercury emissions on the marine mercury cycle and ecosystems.

1. Introduction

29

30

31

32

33

34 35

36

37

38 39

40

41

42

43 44

45

46 47

48

49

50

51

52

53 54

55

56

57

Mercury is a ubiquitous toxic pollutant that <u>can cycle</u> among atmospheric, aquatic, and terrestrial environments (Mason et al., 2012; Lamborg et al., 2014). Anthropogenic discharge of mercury can be transported into marine atmospheres, subsequently entering oceans via wet and

58	dry depositions, constituting a primary source of marine mercury (Outridge et al., 2018). A fraction	Field C	ode Changed
59	of mercury that enters oceans can undergo methylation and bioaccumulate in the food chain, thereby		
60	posing health risks to humans through the consumption of methylmercury-contaminated seafood;		
61	another fraction converts to dissolved gaseous mercury and can escape from surface seawater		
62	through sea-air exchange processes (Lavoie et al., 2018; Obrist et al., 2018). This sea-air exchange	Field C	ode Changed
63	is pivotal to the biogeochemical cycling of mercury, as it influences mercury concentrations in		
64	seawater, oceanic mercury accumulation rates, and methylmercury production (Mason et al., 2017;	Field C	ode Changed
65	Ci et al., 2016). Simultaneously, the sea-air exchange of mercury represented the largest flux		
66	between different environmental media within the global mercury cycle. Previous estimates		
67	indicated that the release of gaseous elemental mercury from the global ocean contributed		
68	approximately one-third of the global atmospheric mercury emissions (Horowitz et al., 2017).	Field C	ode Changed
69	Numerous studies have emphasized the impact of anthropogenic sources on marine		
70	atmospheric mercury. For instance, one study conducted over the Bohai Sea revealed that the		
71	increased concentration of gaseous elemental mercury (GEM) resulted from the long-range		
72	transport of mercury released from anthropogenic sources (Wang et al., 2020). An island	Field C	ode Changed
73	investigation over the East China Sea showed the outflow from mainland China was the primary		
74	contributor to atmospheric GEM (Fu et al., 2018). Cruises campaigns over the East China Sea and	Field C	ode Changed
75	South China Sea observed elevated GEM concentrations at sites proximate to mainland China,		
76	indicating the prominent influence of terrestrial emissions (Fu et al., 2010; Wang et al., 2016a).	Field C	ode Changed
77	Additionally, studies in the Gulf of Mexico, North Atlantic Ocean, and Mediterranean Sea also		
78	attributed significant portions of atmospheric mercury to anthropogenic emissions (Obrist et al.,	Field C	ode Changed
79	2018). Although isotopic signatures have been widely applied to source apportionment of		
80	atmospheric mercury, current isotopic methods still exhibit significant uncertainties due to the poor		
81	understanding of isotopic compositions of gaseous elemental mercury emitted from various sources		
82	and fractionation processes of Hg isotopes during atmospheric transformations (Fu et al., 2018).	Field C	ode Changed
83	Additionally, this approach requires specialized isotopic measurements unavailable for routine		
84	monitoring. At present, quantitative analyses of anthropogenic contributions to marine atmospheric		
1			

 $\underline{mercury\ remain\ limited}. \underline{However, these\ studies\ primarily\ provided\ qualitative\ assessments\ without}$

quantitatively elucidating the contribution of anthropogenic sources to marine atmospheric mercury.

85

Although annual global anthropogenic atmospheric mercury emissions have been approximated to reach 2300 tons, accounting for about one-third of global atmospheric mercury emission (Pirrone et Field Code Changed al., 2010; Zhang et al., 2016), the specific contributions to marine atmospheric mercury remained poorly delineated, thereby constraining insights into the oceanic mercury cycling dynamics. In this regard, it is imperative to develop methodologies capable of quantifying the contributions from anthropogenic sources to marine atmospheric mercury, particularly in critical marginal seas, which served as essential biogeochemical interfaces between landmasses and open oceans. Previous studies have indicated that the importance of the mercury cycling in offshore ecosystems approximated that within open oceanic environments (Fitzgerald et al., 2007). Marginal seas Field Code Changed functioned not only as natural sinks for terrestrial mercury but also represented significant sources of atmospheric mercury (Ci et al., 2011). Given that China ranks as the foremost global emitter of Field Code Changed anthropogenic atmospheric mercury (Pacyna et al., 2016; Pacyna et al., 2010; Zhang et al., 2015), Field Code Changed its emissions inevitably exert profound influences on adjacent marginal seas. Anthropogenic inputs influenced not only the concentrations of atmospheric mercury but also the dynamics of mercury sea-air exchange. Given that Hg⁰ in the surface oceanic waters frequently exceeded its saturation levels, the prevailing direction of sea-air exchange was predominantly upward, facilitating the efflux of mercury from the ocean to the atmosphere (Andersson et al., 2008b; Field Code Changed Mason et al., 2001; Huang and Zhang, 2021). The sea-air exchange of Hg⁰ was governed by the concentration gradients at the atmosphere-seawater interface (Soerensen et al., 2013), which were Field Code Changed influenced by the spectrum of physical and chemical processes within seawater, as well as meteorological conditions and ambient GEM concentrations (Costa and Liss, 1999; Mason, 2009; Field Code Changed Selin, 2009). Previous studies illuminated the direct impact of dissolved gaseous mercury (DGM) in surface waters on Hg⁰ fluxes, while photochemical reduction of Hg (II) has been identified as the principal mechanism driving the DGM generation in marine settings (Amyot et al., 1994; Huang Field Code Changed and Zhang, 2021). Field measurements observed nocturnal peaks in DGM and Hg⁰ fluxes, implying Field Code Changed that dark reduction processes may significantly contribute to these dynamics (O'driscoll et al., 2003; Fu et al., 2013). Hg⁰ fluxes increased 2-4 folds as a result of strengthened wind speeds coupled with Hg (II) inputs from atmospheric precipitation in the Intertropical Convergence Zone (ITCZ) region

Field Code Changed

(Soerensen et al., 2014). While considerable research has elucidated the factors influencing the

87

88

89

90

91

92

93

94

95 96

97

98

99

100

101

102

103

104

105

106

107

108

109

110

111

112

113

114

mercury sea-air exchange, few studies have comprehensively explored the repercussions of fluctuating GEM concentrations on Hg⁰ sea-air dynamics. Given the backdrop of observed annual declines in GEM concentrations(-0.011±0.006 ng m⁻³ y⁻¹) across most Northern Hemispheric regions from 2005 to 2020 (Feinberg et al., 2024) and particularly pronounced declines (-0.29 ng m⁻³) in China from 2013 to 2017 (Liu et al., 2019), conducting such study in marginal seas is essential.

Under the influence of Chinese mainland emissions, mercury pollution in its adjacent marginal seas, such as the East China Sea, Yellow Sea, and Bohai Sea, exhibited pronounced severity. The East China Sea and Yellow Sea, as semi-enclosed seas, are located in the downwind region of East Asia and serve as a major pathway for the transport of pollutants to the Pacific Ocean. The Bohai Sea, as an inland sea, has received a substantial amount of pollutants from the Chinese mainland, making it one of the most mercury-polluted seas in the world (Luo et al., 2012). By focusing on the marginal seas surrounding China, this study integrated observations from two offshore islands, one research cruise, and a coastal city, to reveal the spatiotemporal distribution characteristics of total gaseous mercury (TGM) and dissolved gaseous mercury (DGM). The impact of oceanic meteorological conditions on the atmospheric mercury over the ocean was explored, particularly examining the effects of anthropogenic sources transported from the mainland. Furthermore, we developed a method to quantify the contributions from anthropogenic sources to marine atmospheric mercury and ultimately assessed how these inputs shaped the mercury sea-air exchange dynamics.

2. Methods

2.1 Study area

The study area, illustrated in Figure 1a, encompasses the Bohai Sea (BS), the Yellow Sea (YS), and the East China Sea (ECS). The BS, a shallow inner sea bordered by Liaoning, Hebei, and Shandong provinces, covers around 77×10^3 km². The YS, situated between mainland China and the Korean Peninsula, covers around 38×10^4 km². The ECS, a semi-enclosed marginal sea positioned downwind of East Asia, extends over 77×10^4 km². Field measurements were conducted at Juchua Island (JHI) in the BS, approximately 10 km from Xingcheng City, Liaoning Province. Due to its proximity to the mainland, JHI experienced marked impacts from anthropogenic emissions (Li et

Field Code Changed

Field Code Changed

Field Code Changed

al., 2023). Field measurements were also conducted at Huaniao Island (HNI) in the ECS, approximately 80 km from Shanghai. Although local anthropogenic emissions were negligible there, this island was frequently affected by terrestrial transport during winter and spring, when prevailing northwesterly winds dominated (Fu et al., 2018; Qin et al., 2016). A cruise campaign was conducted aboard the research vessel (R/V) Dongfanghong III. The cruise routes, as shown in Figure 1a, covered most of the YS and ECS regions. Land-based measurements were conducted at a super site (Dianshan Lake, DSL) in the rural Shanghai Qingpu District. This super site is located at the intersection of Shanghai, Zhejiang, and Jiangsu provinces.

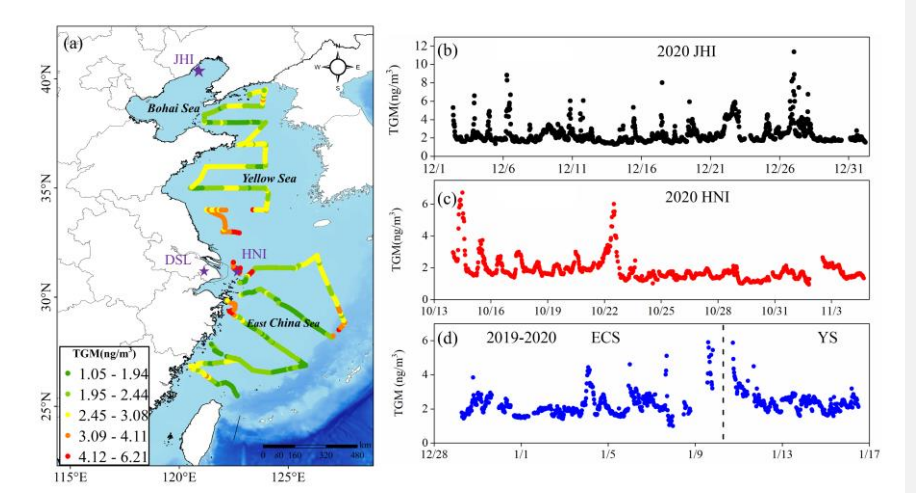


Figure 1. (a) The locations of two island sites (JHI and HNI) and one inland site (DSL) denoted by purple pentagrams. The spatial distribution of TGM concentrations over the East China Sea (ECS) and the Yellow Sea (YS) is shown along the cruise routes. The time series of TGM concentrations are measured at (b) JHI, (c) HNI, and (d) ECS+YS, respectively.

2.2 TGM/GEM measurements

TGM measurements were performed utilizing a modified Tekran 2600 instrument across various locations and timeframes, i.e., JHI from December 2, 2020 to January 1, 2021, HNI from October 14 to November 4, 2020, and aboard the research vessel (R/V) Dongfanghong ||| from December 29, 2019 to January 16, 2020. The Tekran 2600 monitor operated similarly to Tekran

Field Code Changed

Formatted: Font: Not Italic

Formatted: Font: Not Italic

2537B, which is widely used for continuous collection and analysis of atmospheric mercury (Sprovieri et al., 2016; Landis and Keeler, 2002). During the operation of the modified Tekran 2600, atmospheric mercury was adsorbed onto the first gold trap over a 24-minute sampling period. After sampling, the mercury on the first gold trap was thermally desorbed and transferred to the second gold trap. The second trap was then analyzed by the detector during a 6-minute detection phase, resulting in an overall 30-minute sample resolution. To ensure data quality during cruise observations, the instrument was calibrated daily using the external calibration unit Tekran 2505. Samples were pre-dried via a soda lime drying tube prior to detector entry to prevent humidity interference. In this Tekran 2600 setup, sampling air passed through a Teflon filter to remove particulate matters, thereafter passing through a drying tube filled with soda lime to eradicate moisture prior to TGM collection in a gold tube. Following sample acquisition, the gold tube was heated to release Hg, which was subsequently analyzed using cold vapor atomic fluorescence spectroscopy (CVAFS) with argon as the earrier gas. Sampling intervals and flow rates were preset at 30 min and 500 ml/min, respectively. Calibration of the instrument was performed using the external calibration unit Terkan 2505 every 24 hours, _ensuring that measured recovery rates exceeded 95% during each calibration cycle. Additionally, the drying tube and Teflon filter underwent replacement bi-weekly to maintain optimal performance. GEM measurements were conducted at DSL in Shanghai from October to December,

165

166

167

168

169

170

171

172

173

174

175

176

177

178

179

180

181

182

183 184

185

186

187

188

189

190

191

192

193

2020March 1, 2015 to February 28, 2019, employing the atmospheric mercury monitoring system (Tekran 2537B/1130/1135) as documented in our prior study (Qin et al., 2020). Briefly, GEM was captured utilizing dual gold cartridges at a flow rate of 1.0 LPM and 5-minute intervals. Subsequently, GEM underwent thermal decomposition for detection via CVAFS. During the sampling process, rigorous quality controls were applied. Prior to sampling, denuders and quartz filters were duly prepared and cleansed adhered to Tekran technical directives. To ensure accuracy, calibration was routinely executed every 47 hours using an internal permeation source, alongside manual injections of standard saturated mercury vapor₅. For the Tekran 2537B, the average duplication rate between the A and B traps is 99%, with deviations between the two traps consistently below 3%. To mitigate the impact of high humidity on the instrument, samples are first passed through a soda lime drying tube for dehumidification before entering the detector. Further,

Field Code Changed

Formatted: Font: 10.5 pt

Formatted: Font: 10.5 pt

the KCl-coated denuder, Teflon-coated glass inlet, and impactor plate were swapped weekly, while the quartz filters underwent monthly replacement.

It is noteworthy that TGM in the atmosphere comprises GEM and GOM (gaseous oxidized mercury). Generally, GEM constitutes over 95% of atmospheric mercury (Mao et al., 2016), particularly in the marine boundary layer, including China's marginal seas (Wang et al., 2016b; Fu et al., 2018; Ci et al., 2011; Wang et al., 2019a). Therefore, this study does not differentiate between TGM and GEM, conforming to analogous treatments in existing research (Fu et al., 2018; Ci et al., 2011).

2.3 DGM measurement

DGM (dissolved gaseous mercury) collection from seawater adhered to the procedure described in previous studies (Gardfeldt et al., 2003; O'driscoll et al., 2003). The sampling process involved the following steps. 1.5 L of surface seawater was collected in a Teflon bottle and subsequently transferred into a borosilicate glass bottle. An introduction of free-Hg argon at approximately 500 ml/min purged the seawater for 60 minutes to extract the DGM onto a gold trap, aided by a soda lime tube deployed to extract water vapor prior to the gold trap. The gold trap was maintained at ~50°C during extraction to prevent water vapor condensation. The DGM stored in the gold trap was measured using the Tekran 2600 post-sampling. To assure quality, stringent assurance and control measures were enacted through replicated field blank experiments. DGM excised from an equivalent volume of Milli-Q water served as the analytical system blank, encompassing a total of 12 blank experiments during field samplings at JHI and HNI, as well as during the R/V measurements. The mean system blank calculated was 2.5±1.3 pg/L (n = 20), with a detection limit of 3.4 pg/L.

2.4 Ancillary data

At JHI, water-soluble ions in PM_{2.5}, including sulphate (SO₄²), nitrate (NO₃⁻), ammonium (NH₄⁺), chloride (Cl⁻), sodium (Na⁺), potassium (K⁺), magnesium (Mg²⁺), calcium (Ca²⁺), alongside the soluble gases such as ammonia (NH₃) and sulfur dioxide (SO₂) were continuously monitored using an In-situ Gas and Aerosol Composition monitoring system (IGAC) (Wang et al., 2022).

Field Code Changed

Field Code Changed

Field Code Changed

Field Code Changed

IGAC operated at a 1-hour temporal resolution and consisted of a wet annular denuder (WAD) and ion chromatography (IC) equipped with columns CS17 and CG17 for cations and AG11-HC and AS11-HC for anions. Ambient air was drawn into a PM_{2.5} cyclone inlet by a built-in pump at a flow rate of 16.7 L/min. The sampled air was separated by passing through the vertically placed WAD to capture water-soluble gases, and airborne particles were collected by a steam scrubber and impact aerosol collector placed downstream. Air samples were dissolved by 30 ml ultra-pure water (18.25 $M\Omega$ cm⁻¹) and then divided into two steams. Both aqueous samples (including particles and gases) were injected into the IC system by two separated syringe pumps for analyzing the cations and anions. For quality assurance/quality control (QA/QC) of IGAC, a standardized lithium bromide (LiBr) solution was continuously introduced into aerosol liquid samples during the campaign to validate sampling and analytical stability. Weekly calibrations were performed for the ion chromatography (IC) module using certified standard solutions, with linearity (R² > 0.99) and detection limits (LODs) validated. Black carbon (BC) in PM2.5 was measured continuously using a multi-wavelength Aethalometer (AE-33, Magee Scientific, USA). Meteorological parameters were measured using a Vaisala WXT530 surface weather station (Vaisala, Finland). Surface seawater temperature was recorded by a YSI EC300 portable conductivity meter (YSI, USA) with a resolution of 0.1°C. Meteorological data (e.g., air temperature, wind speed/direction) were observed using a co-located Pulsed Coherent Doppler Lidar (PCDL, Wind3D 6000) and a temperature/humidity sensor (YGC BYX M). The surface seawater temperature was measured by a salinity, conductivity and temperature meter (YSI EC300).

223

224

225

226

227

228

229

230

231

232

233

234

235

236

237

238

239

240

241 242

243

244

245

246

247

248

249

250

251

Formatted: Font: Not Italia

At HNI, meteorological parameters were gathered using an automatic weather station (AWS).

Methods—methods for analyzing meteorological parameters, BC, and the—surface seawater temperature mirrored those employed at JHI.

During the cruise campaign, the meteorological metrics (e.g., air temperature, wind speed/direction) and surface seawater temperature were collected from the Finnish Vaisala AWS430 shipborne weather station instrumentations onboard the R/V. AE-33 was also used for BC measurements during the cruise.

At DSL, water-soluble ions in PM_{2.5} and soluble gases were also measured by the IGAC instrument. Trace metals in PM_{2.5} (Al, Ti, V, Cr, Mn, Fe, Co, Ni, Cu, Zn, Ga, As, Sr, Cd, Sn, Sb,

Formatted: Font: 10.5 pt, Not Italic

Formatted: Font: 10.5 pt

Formatted: Font: 10.5 pt, Not Italic

252 Ba, Tl, Pb, and Bi), were continuously measured using an Xact multi-metals monitor (Model XactTM 253 625, Cooper Environmental Services LLT, OR, USA). It operated at a flow rate of 16.7 L min⁻¹ 254 with hourly resolution. Particles in the airflow passed through a PM2.5 cyclone inlet and were 255 deposited onto a Teflon filter tape, then the samples were transported into a spectrometer for analysis 256 via nondestructive energy-dispersive X-ray fluorescence. 257 Planetary boundary layer (PBL) height data were obtained from the Global Data Assimilation 258 System (GDAS) archive maintained by the U.S. National Oceanic and Atmospheric Administration (NOAA), available through the READY (Real-time Environmental Applications and Display 259 sYstem) portal (https://www.ready.noaa.gov/archives.php; last accessed: 11 May 2025). The dataset. 260 261 featuring 1-hour temporal resolution, was processed and extracted using MATLAB R2021b 262 (MathWorks, Natick, MA). 263 264 265 2.5 Positive matrix factorization (PMF) 266 The PMF model is recognized for its efficacy in elucidating sources profiles and quantifying source contributions (Paatero and Tapper, 1994). The underlying principle of PMF posits that 267 268 sample concentration is dictated by source profiles with disparate contributions, mathematically 269 represented as: $X_{jj} = \sum_{k=1}^{P} g_{jk} f_{kj} + e_{jj}$ (1) 270 where Xij represents the concentration of the jth species in the jth sample, gik is the contribution of 271 272 the kth factor in the ith sample, fki provides the information about the mass fraction of the jth species 273 in the kth factor, eij is the residual for specific measurement, and P represents the number of factors. 274 The objective function, defined in Eq. (2) below, represents the sum of the squared differences 275 between measured and modeled concentrations, weighted by concentration uncertainties. Minimizing this function allows the PMF model to determine optimal non-negative factor profiles 276 277 and contributions: $Q = \sum_{i=1}^{n} \sum_{j=1}^{m} \left(\frac{x_{ij} - \sum_{k=1}^{p} A_{ik} F_{kj}}{S_{ij}} \right)^{2} (2)$ 278 Where X_{ii} denotes the concentration of the jth pollutant in the ith sample, A_{ik} represents the 279

Formatted: Font: 10.5 pt, Not Italic Formatted: Font: 10.5 pt Formatted: Font: Not Italia Field Code Changed Formatted: Font: Not Italia Formatted: Font: Not Italia Formatted: Font: 10.5 pt Formatted: Font: Not Italia Formatted: Font: Not Italia Formatted: Font: Not Italia Formatted: Font: Not Italia Formatted: Font: Not Italic Formatted: Font: Not Italia Formatted: Indent: First line: 2 ch Formatted: Centered Formatted: Font: Not Italia

Formatted: Font: 10.5 pt

contribution of the kth factor to the ith sample, Fki is the mass fraction of the jth pollutant in the jth

281	pollutant in k^{th} factor, S_{ij} is the uncertainty of the j^{th} pollutant in the i^{th} sample, and p is the number			
282	of factors. Detail description can be seen in the previous study (Paatero and Tapper, 1994),		Formatted	
283	TGM, air temperature (unit: Kelvin), gaseous pollutants, and major aerosol chemical species		Formatted: Indent: First line: 2 ch	
284	were used as inputs for the PMF model. We tested factor numbers ranging from 3 to 8, with the		Formatted	
285	optimal solution determined by analyzing the slope of the Q-value versus factor count. Model			
286	stability was assessed through residual analysis, correlation coefficients between observed and			
287	predicted concentrations, and Q-value trends. A six-factor solution in DSL and a five-factor solution	//		
288	inat JHI provided the most stable and interpretable results.	/		
289	Detail description can be seen in the previous study At Dianshan Lake (DSL), we selected		Formatted: Font: 10.5 pt	
290	observational data from October to December, 2020 (totaling 1,080 valid data points) for PMF			
291	modeling to align with the HNI observational campaign. For Juehua Island (At JHI), observational			
292	data from December 2 to 30, 2020 (totaling 675 valid data points) were used for PMF analysis.			
293				
294	2.6 Sea-air exchange flux			
295	The sea-air exchange fluxes of Hg ⁰ were calculated via the following equation (Andersson et		Field Code Changed	
296	al., 2008a; Wanninkhof and Oceans, 1992; Wangberg et al., 2001):			
297	$F = K_{M}(C_{W} - C_{\alpha}/H') $ (23)		Formatted: Font: 10.5 pt	
298	where F is the sea-air exchange flux, K_w represents the gas exchange velocity, C_w and C_a represent		Formatted	
299	the DGM concentration in seawater and the TGM concentration in the atmosphere, respectively, H'			
300	is the dimensionless Henry's law coefficient of Hg^0 between the atmosphere and seawater. $K_{\rm w}$ is			
301	calculated as follows (Soerensen et al., 2010b; Nightingale et al., 2000).		Field Code Changed	
302	$K_{\rm w} = 0.31 u_{10}^2 (S_{\rm CHg}/660)^{-0.5}$ (34)		Formatted	
303	where u_{10} is 10-meter wind speed, $S_{C_{Hg}}$ is the Schmidt number of Hg^0 , 660 is the Schmidt number			
304	of CO ₂ in 20 °C seawater (Poissant et al., 2000). The Schmidt number for Hg (S _{CHg}) was calculated		Field Code Changed	
305	as:		Formatted: Subscript	
306	$S_{C_{Hg}} = v/D_{Hg} $ (5)		Formatted: Centered	
207			Formatted	(
307	where v is seawater kinematic viscosity (Wanninkhof, 2014) and D _{Hg} is the diffusion coefficient of		Field Code Changed	
308	Hg (Kuss et al., 2009).		Formatted: Subscript	
			Field Code Changed	

H' is calculated as follows (Andersson et al., 2008a).

 $H' = \exp(-2403.3/T + 6.92)$ (46)

Where T is the surface seawater temperature in K.

3. Results and Discussions

309

310

311

312 313

314

315

316

317

318

319

320

321

322

323

324

325

326

327

328

329

330

331

332

333

334

335

336

337

3.1 Characteristics of TGM over Chinese marginal seas

campaigns, including December 2, 2020 to January 1, 2021 at Juehua Island (JHI), October 14, 2020 to November 4, 2020 at Huaniao Island (HNI), and December 29, 2019 to January 16, 2020 over the Yellow Sea and East China Sea (YS/ECS). The mean TGM concentrations during the three periods were 2.32 ± 1.02 ng/m³, 1.85 ± 0.74 ng/m³, and 2.25 ± 0.66 ng/m³, respectively. TGM at JHI exhibited pronounced fluctuations, frequently surpassing high values of 6 ng/m³, which was attributed to the enhanced coal combustion for residential heating in winter (Li et al., 2023). Conversely, TGM at HNI and across the YS/ECS demonstrated less fluctuations, with concentrations predominantly remaining below 6 ng/m³. The cruise campaign unveiled the spatial distribution of TGM over the ocean (Figure 1a), generally showing its decreasing trend with the increased distance away from the continent. Specifically, hot spots were observed in the eastern oceanic region of Jiangsu province, the Changjiang estuary, and the outer sea close to the Hangzhou Bay. The continental outflows likely explained this phenomenon. The mean TGM concentrations reached 2.36 ± 0.65 ng/m³ and 2.16 ± 0.81 ng/m³ over the Yellow Sea and East China Sea, respectively, significantly higher than the background level in the Northern Hemisphere (1.58 ± 0.31) ng/m³) (Bencardino et al., 2024) The mean TGM concentrations reached 2.36 ± 0.65 ng/m³ and 2.16 ± 0.81 ng/m³-over the Yellow Sea and East China Sea, respectively, significantly higher than the background level in the Northern Hemisphere (Sprovieri et al., 2016) and also surpassing measurements recorded in the other open ocean areas such as the South China Sea (1.52±0.32 ng/m³), Mediterranean Sea (1.8± 1.0 ng/m³), Bering Sea (1.1 ± 0.3 ng/m³), Pacific Ocean (1.15-1.32ng/m³), and Atlantic Ocean (1.63 ± 0.08 ng/m³)also surpassing measurements recorded in the other open ocean areas such as the South China Sea, Mediterranean Sea, Bering Sea, Pacific Ocean, and Atlantic Ocean (Laurier and Mason, 2007; Soerensen et al., 2010a; Mastromonaco et al., 2017;

Figure 1b-d shows the time series of TGM concentrations measured during three field

Formatted: Font: 10.5 pt
Formatted: Font: 10.5 pt

Field Code Changed

Formatted: Font: 10.5 pt

Field Code Changed

Field Code Changed

Formatted: Font: 10.5 pt

Kalinchuk et al., 2018; Wang et al., 2019b). 72h air mass backward trajectory analyses revealed that air masses over the YS predominantly originated from Liaoning and Inner Mongolia province in northern China, whereas trajectories over the ECS were largely dispersed across the ocean and Eastern China (Figure S1). This divergence may be one of the reasons why the TGM concentration in the YS was higher than that in the ECS. This divergence elucidated the elevated TGM concentrations over the YS compared to the ECS.

338

339

340

341

342

343

344

345

346

347

348

349

350

351

352

353

354

355

356

357

358

359

360

361

362

363

spatial scale.

The diurnal variations of TGM concentrations along with ambient temperature and sun flux during the three periods are displayed in Figure 2. At HNI, TGM commenced increasing at 7:00 a.m., peaking at around 2.44 ng/m³ by 12:00, subsequently declining and stabilizing post 6:00 p.m. The mean TGM concentration during daytime (06:00-18:00) ($2.00 \pm 0.80 \text{ ng/m}^3$) surpassed that of nighttime (1.66 \pm 0.40 ng/m³) (t test, p < 0.001). The TGM diurnal pattern displayed strong concordance with temperature and solar flux (Figure 2a), indicative of significant impacts from natural sources (Osterwalder et al., 2021; Huang and Zhang, 2021; Mason et al., 2001), The TGM diurnal pattern displayed strong concordance with temperature and solar flux (Figure 2a), indicative of significant impacts from natural sources. At JHI (Figure 2b), TGM also rose around early morning and peaked at 2.65 ng/m³ by 10:00 a.m., with nocturnal levels markedly increasing from 2.12 ng/m³ at 6:00 p.m. to 2.60 ng/m3 at 11:00 p.m. During daytime, TGM generally showed consistent variation with temperature and sun flux, indicating the influence of natural mercury release. However, the notable frequency of nocturnal peaks suggested that in addition to natural sources, TGM measured at JHI was also significantly affected by anthropogenic sources and unfavorable atmospheric diffusion conditions, specifically from coal combustion for the winter residential heating in northern China (Li et al., 2023). The diurnal pattern of TGM throughout the cruise campaign diverged from those of HNI and JHI, lacking a consistent relationship with temperature and sun flux. This was mainly due to that the cruise sampling was variable in both the temporal and Formatted: Font: 10.5 pt

Formatted: Font: Not Italic

Formatted: Font: Not Italic

Formatted: Font: 10.5 pt

Formatted: Font: 10.5 pt

Formatted: Font: 10.5 pt

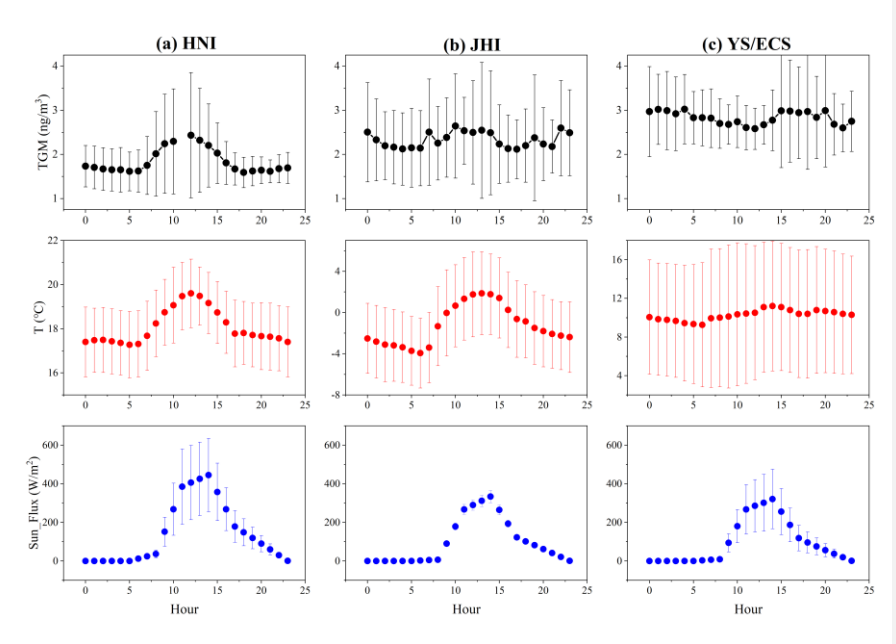


Figure 2. Diurnal variations of TGM, ambient temperature and sun flux at (a) HNI, (b) JHI, and (c) the YS/ECS cruise, respectively.

Positive correlations between TGM concentrations and ambient temperature at both HNI and JHI were observed, yielding R² values of 0.53 and 0.60, respectively (Figure 3a&3b). Since temperature played a crucial role in Hg⁰ release from natural surfaces (Lindberg et al., 1998; Poissant et al., 2000), the evident correlation between TGM and temperature exemplified the significant effects of natural surface emissions.

Positive correlations were also observed between TGM, relative humidity, and wind speed at both HNI and JHI (Figure 3). Previous studies suggested wetting processes may promote the reduction of Hg⁺⁺ to Hg⁰ in surface seawater, while higher wind speed accelerated its evasion (Lin et al., 2010b; Soerensen et al., 2013). Previous studies suggested wetting processes may promote the reduction of Hg⁺⁺ to Hg⁰ in soil and water, while high wind speed favored the escape of Hg⁰ from soils (Lin et al., 2010a; Wanninkhof and Oceans, 1992; Pannu et al., 2014). This may explain the observed positive correlations between humidity, wind speed, and TGM concentrations. Thus, relative humidity and wind speed were verified as critical factors influencing to the levels of TGM as similar as temperature.

Formatted: Font: 10.5 pt, Font color: Red

Field Code Changed

Formatted: Font: 10.5 pt

At HNI, TGM increased concurrently with rising Planetary Boundary Layer (PBL) heights from around 380 to 1000 m, yet decreased with further increase in PBL beyond around 1000 m (Figure 3a). This observed diurnal pattern of TGM may primarily stem from the interplay between temperature-driven natural surface emissions and atmospheric dilution effects. When the PBL height was below 1 km, its increase coincided with rising temperature. Under these conditions, the enhancement of natural surface emissions due to temperature outweighed the dilution effect caused by the developed PBL, leading to increased TGM concentrations. Afterwards, as the PBL height continued to rise, the dilution effect gradually surpassed the temperature-driven emission enhancement, resulting in a decline of TGM concentrations. This was likely due to that the gradual increase in the PBL height from night to day corresponded with amplifying natural surface emissions of mercury. When PBL was below around 1km, the dilution effect due to heightened PBL could not counterbalance the enhanced natural surface emissions. In contrast, the similar phenomenon lacked manifestation at JHI, where TGM concentrations decreased with the increase of PBL (Figure 3b). Due to the significantly lower marine mercury emissions in the BS (Wang et al., 2020), than in the ECS (Wang et al., 2016a), This this phenomenon was likely ascribed to that the natural release around JHI was weaker than that around HNI, thus the dilution effect of elevated PBL overwhelmed the effect of natural surface emissions. Compared to HNI and JHI, the cruise campaign showed almost no relationship between TGM and temperature, relative humidity, wind speed, or PBL height were identified (Figure 3c), which shared similar reasons as discussed in the diurnal variation of TGM.

382

383

384

385

386

387

388

389

390

391

392

393

394

395

396

397

398

399

400

401

402

Formatted: Font: 10.5 pt

Formatted: Font: 10.5 pt
Formatted: Font: 10.5 pt
Formatted: Font: 10.5 pt
Formatted: Font: 10.5 pt
Formatted: Font: 10.5 pt
Formatted: Font: 10.5 pt
Formatted: Font: 10.5 pt

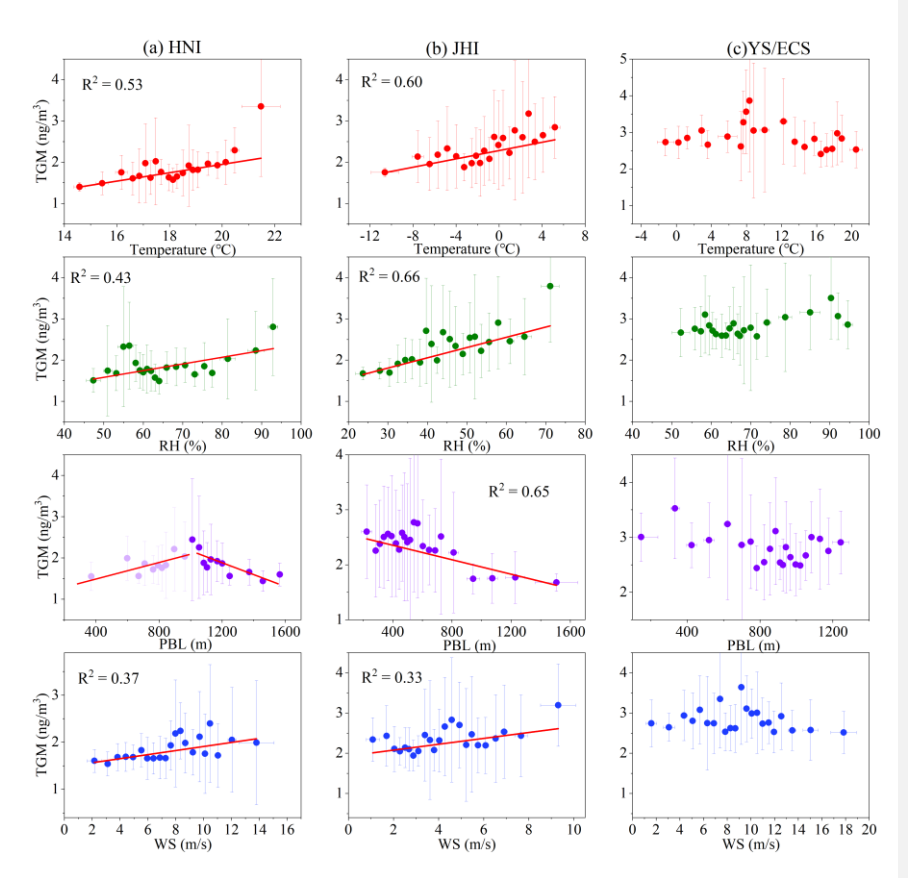


Figure 3. Relationship between TGM concentration and temperature, relative humidity, planetary boundary layer height, and wind speed at (a) HNI, (b) JHI, and (c)YS/ECS, respectively.

3.2 Influence of continental outflows on marine TGM

The potential source regions of TGM at HNI and JHI are illustrated in Figure S2. At HNI, TGM mainly derived from the lands of Jiangsu Province and vast coastal waters of the East China Sea. While at JHI, the hot spots of TGM were mainly located in the southern Mongolia and Beijing-Tianjin-Hebei regions. This indicated that the relatively high TGM concentrations at the coastal islands were closely related to the continental outflows. Using HNI as an example, Figure S3 compares the daily mean TGM concentration at HNI with the daily mean concentrations of CO, SO₂, and PM_{2.5} in nearby coastal cities including Zhoushan, Ningbo, Jiaxing, Shanghai, and Ningbo. Consistently temporal variations were observed between TGM and these pollutants, particularly for

the peak concentrations, further confirming that offshore TGM concentrations were significantly influenced by continental outflows.

To assess the impact of anthropogenic sources on marine TGM, the daily TGM concentrations at HNI and DSL (a suburban site in the Yangtze River Delta, Figure 1a) were compared (Figure 4a).

Their concentration time series exhibited moderate agreement, suggesting potential land-sea

 $\underline{\text{interactions.}} \ \underline{\text{Good consistency between them was found, indicating strong land sea interactions.}}$

Furthermore, the correlation between TGM and BC at DSL was pronounced (R^2 =0.56, Figure 4b).

This was expected, as BC primarily originated from fossil fuels combustion (Li et al., 2021; Briggs

and Long, 2016), which was also the major anthropogenic source of TGM (Pacyna et al., 2006;

Streets et al., 2011; Liu et al., 2019). In contrast, the correlation between TGM and BC at HNI was

much weaker (R²=0.34, Figure 4c). Being an offshore site, HNI could be more strongly influenced

427 by natural sources than DSL.

416

417

418

419

420

421

422

423

424

425

426

428

429

430

431

432

433

434

435

436

437

438

439

440

441

442

443

444

To qualitatively evaluate the relative importance of anthropogenic and natural sources to TGM, the ratio of TGM/BC was introduced as an indicator with lower ratios implying the prevalence of anthropogenic sources, and vice versa. Figure 4d shows that the TGM/BC ratio at DSL (mean of 1.6 ng μg⁻¹) was substantially lower than that at HNI (5.2 ng μg⁻¹)₂₅ On one hand, lower contribution of anthropogenic sources to TGM in the coastal environment compared to the urban environment was expected. On the other hand, BC deposited more quickly than TGM, thus also elevating the TGM/BC ratios was at locations far from sources. indicating much stronger contribution of natural sources to TGM in the coastal environment than the urban environment. The cruise measurement illustrated the spatial distribution of the TGM/BC ratio over YS/ECS, showing a tendency of decreasing values with increasing distance away from the coasts (Figure 4e). For instance, in the East China Sea, the TGM/BC ratio near the coasts typically ranged from 0.3 to 5.2 ng μg⁻¹, while offshore values generally fluctuated between 8.6 and 22.9 ng µg⁻¹. This further corroborated the important contribution of marine natural emissions to TGM. In regard of different maritime spaces, the northern oceanic regions showed considerably lower values than those in the southern sea regions. In the Yellow Sea, the mean TGM/BC ratio was 4.1 ng µg⁻¹, noticeably lower than that of $6.5 \ ng \ \mu g^{\text{--}1}$ observed in the East China Sea.

Formatted: Font: 10.5 pt

Field Code Changed

Formatted: Font: 10.5 pt, Font color: Red

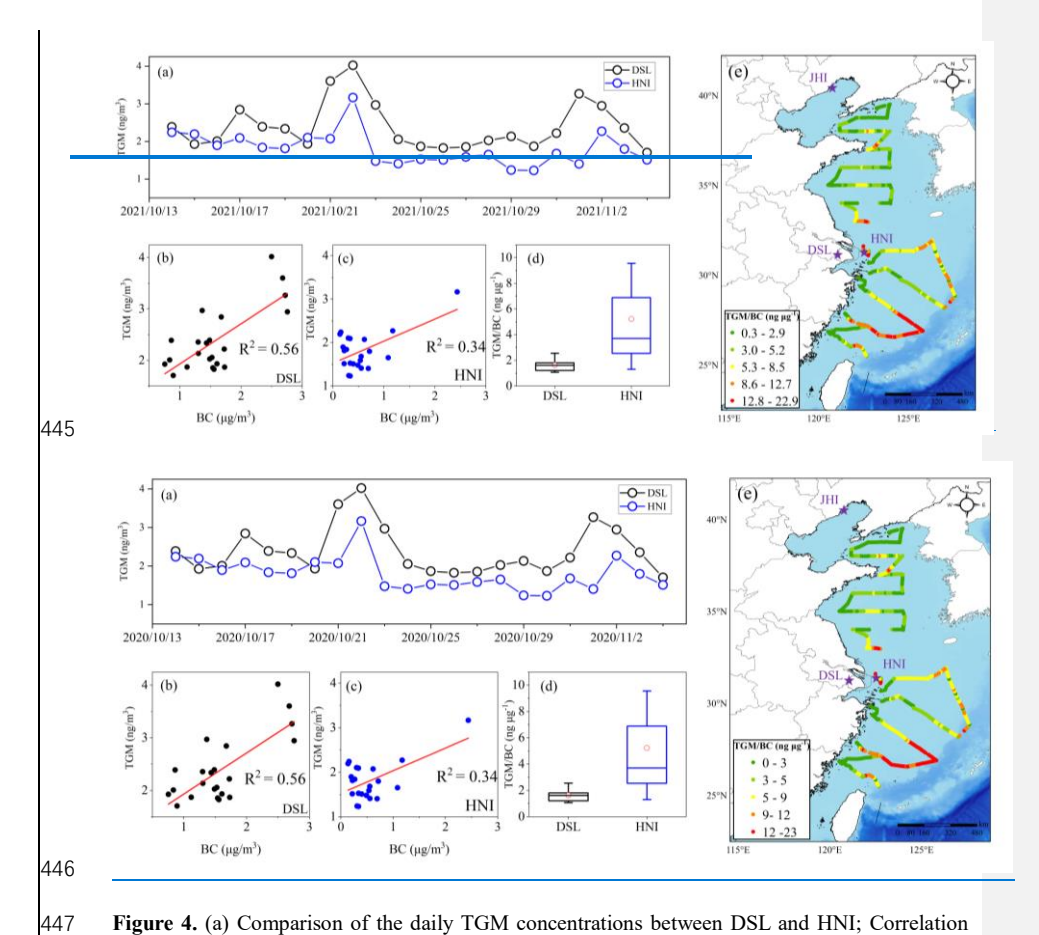


Figure 4. (a) Comparison of the daily TGM concentrations between DSL and HNI; Correlation between TGM and BC at (b) DSL and (c) HNI; (d) Comparison of the TGM/BC ratio between DSL and HNI; (e) Spatial distribution of the TGM/BC ratio along the cruise routes over the ECS and YS.

3.3 Quantification of anthropogenic vs. marine sources to TGM

Based on the discussions above, it is essential to disentangle the anthropogenic and natural sources of atmospheric mercury. Here, the PMF model was employed for the comprehensive dataset obtained at DSL and JHI, respectively. Considering the direct correlation between temperature and natural release of atmospheric mercury (Wang et al., 2014; Zhu et al., 2016) and the indirect correlation between ammonia and natural release of atmospheric mercury (Qin et al., 2019), we utilized temperature and ammonia as indicators of natural atmospheric mercury sources, which has

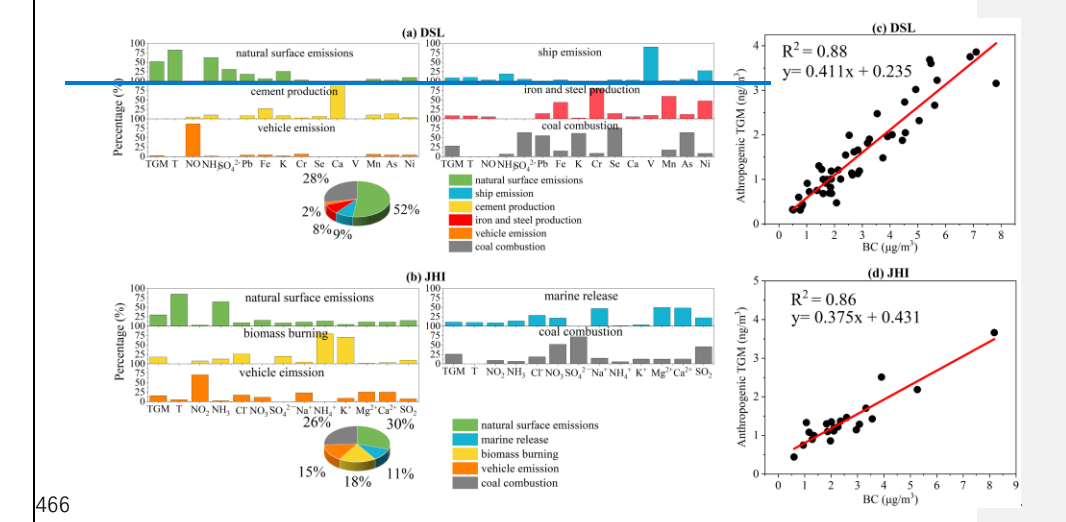
Field Code Changed

been proven feasible (Qin et al., 2020). Inputs for PMF also encompassed SO₄²⁻, Cl⁻, NO₃⁻, Na⁺,

Field Code Changed

NH₄⁺, K⁺, Mg²⁺, Ca²⁺, SO₂, NO, Pb, Fe, K, Cr, Se, Ca, V, Mn, As, and Ni. While running the PMF model, we tested the number of factors from three to eight and determined the optimal solutions through analyzing the slope of the Q values in relation to the number of factors. The analyses revealed that a six-factor solution for DSL and a five-factor solution for JHI produced the most robust and coherent interpretations.





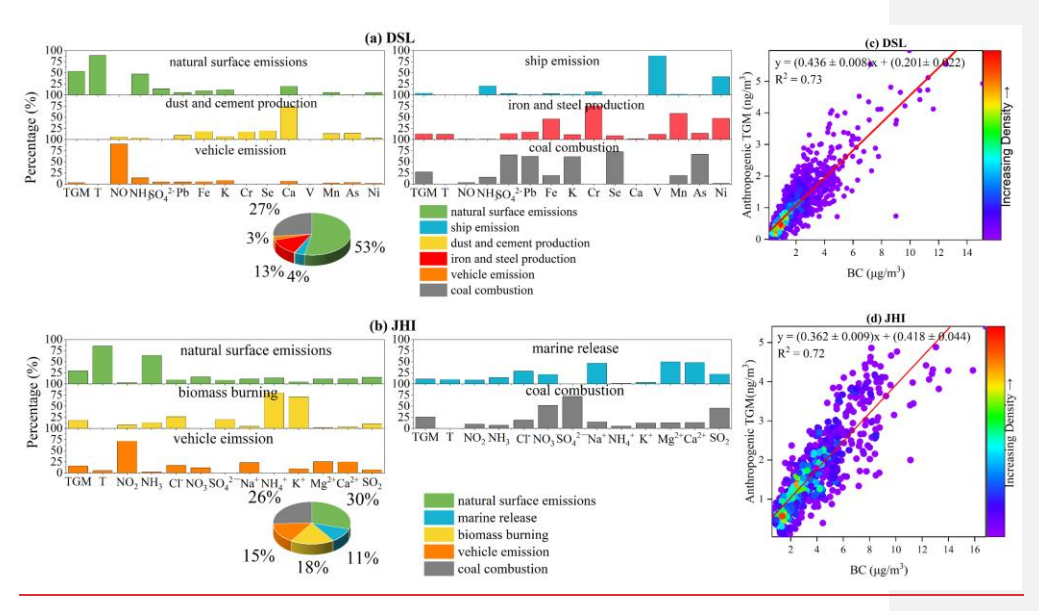


Figure 5. Source apportionment of TGM at (a) DSL and (b) JHI; Linear relationship between BC and anthropogenic TGM at (c) DSL and (d) JHI.

As detailed in Figure 5a, six distinct factors were resolved by PMF at DSL. The factor characterized by high loadings of temperature, NH₃, and TGM represented the natural surface emissions of mercury. A second factor with notable loading of V and moderate loading of Ni was ascribed to be shipping emissions as V has been considered a typical tracer of heavy-oil combustion, which is commonly used in marine vessels (Viana et al., 2009). The dust and cement production was associated with a factor exhibiting prominent Ca loading. The factor displaying high loading of Cr and moderate loadings of Fe and Mn was attributed to iron and steel production. Another factor, categorized by elevated NO levels, was linked to vehicle emissions. Finally, the factor with high loadings of SO₄². Pb, K, Se, and As was indicative of coal combustion. PMF results indicated that the contributions of anthropogenic and natural sources to TGM were approximate 48% and 52% at DSL, respectively. By applying the same PMF modeling strategy at JHI, the contributions of anthropogenic and natural sources to TGM at JHI were 59% and 41%, respectively (Figure 5b). The source apportionment results signified substantial influences of both human and natural factors on TGM levels, with their contributions being nearly equivalent. Furthermore, correlation analysis was

Formatted: Font: 10.5 pt, Not Italic
Formatted: Font: 10.5 pt
Formatted: Font: 10.5 pt, Not Italic
Formatted: Font: 10.5 pt

conducted between the absolute contribution of anthropogenic sources to GEM and BC, yielding a high correlation coefficient (R²) of 0.88 and 0.86 at DSL and JHI (Figure 5c&5d), respectively. It should be noted that BC was not included in PMF modeling, thus the robust relationship between anthropogenic GEM and BC suggested that BC can serve as a viable indicator for quantifying anthropogenic contributions to TGM.

 Based on the results above, the regression formulas obtained from DSL (Anthropogenic TGM = (0.441436 ± 0.008) *BC + (0.235201 ± 0.022) , Figure 5c) and JHI ((Anthropogenic TGM = $0.375362 \pm 0.009)$ *BC + (0.431 ± 0.044) , Figure 5d) were further applied to the cruise observation for the purpose of differentiating the anthropogenic and natural fractions of TGM over the ocean. The following criteria were applied. If the air mass backward trajectories (purple segments in Figure S4) primarily originated from northern China, the JHI-derived formula was employed; If the air mass backward trajectories (green segments in Figure S4) passed through the Yangtze River Delta region or hovered over the East China Sea, the DSL-derived formula was enacted. Due to the uncertainties of regression slopes and intercepts of the regression formulas, this approach caused around 5% uncertainties on differentiating the anthropogenic and natural fractions of TGM.

Time-series of mass concentrations of anthropogenic and natural TGM in different coastal and oceanic regions after applying the above equations are shown in Figure S5. Concentrations of anthropogenic TGM at HNI, JHI, ECS, and YS were $0.61-64\pm0.29-30$ ng/m³, 1.28 ± 0.75 ng/m³, 0.6358 ± 0.454 ng/m³, and 0.9286 ± 0.252 ng/m³, respectively. And the concentrations of natural TGM were 1.158 ± 0.468 ng/m³, 0.88 ± 0.26 ng/m³, 1.549 ± 0.523 ng/m³, and 1.3844 ± 0.513 ng/m³ at the four locations above, respectively. To ensure the reliability of these results, the relationship between natural TGM and temperature was explored, yielding R² of 0.92, 0.76, 0.75, and 0.63 at HNI, JHI, ECS, and YS, respectively (Figure 6). The correlation was significantly stronger than that between the total TGM and temperature, particularly in the ECS and YS regions, where no correlations were observed (Figure 3c). This proved that the quantitative method established above was reliable.

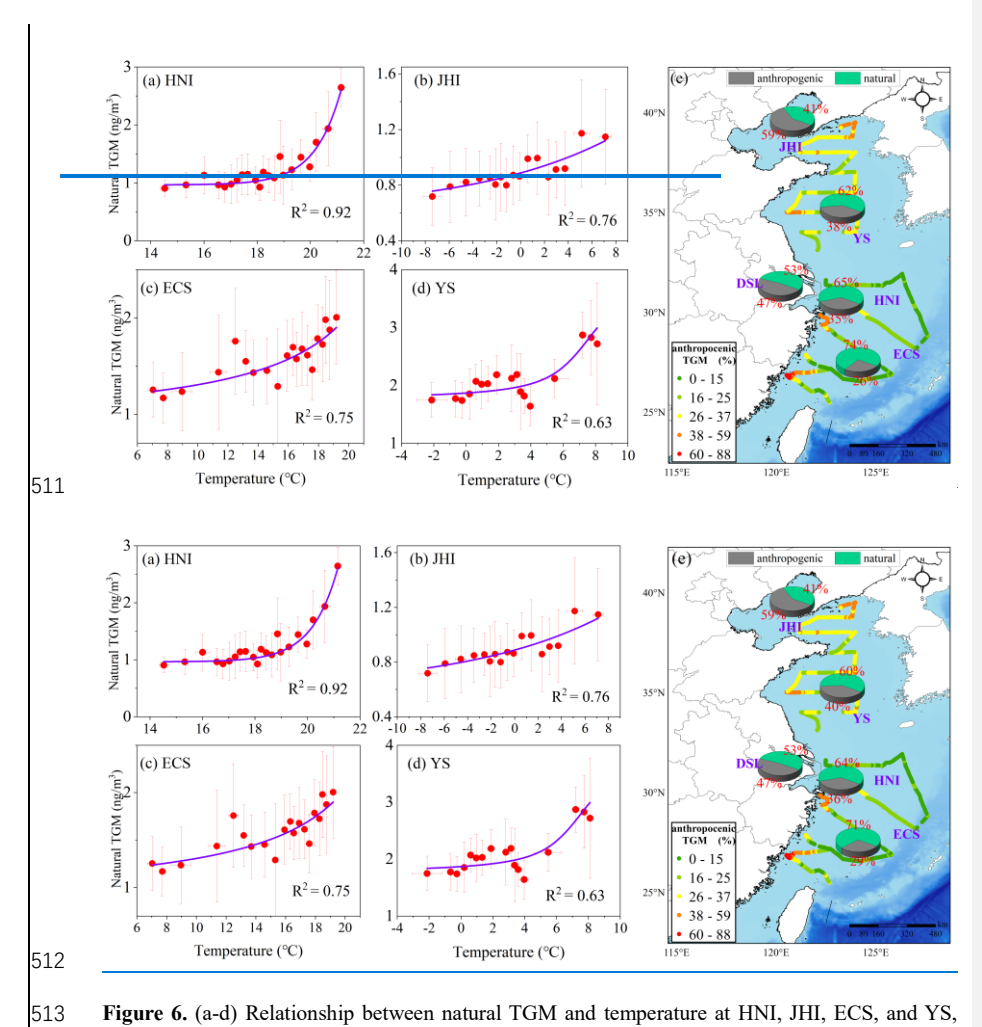


Figure 6. (a-d) Relationship between natural TGM and temperature at HNI, JHI, ECS, and YS, respectively. (e) Spatial distribution of the relative contributions of anthropogenic and natural sources to TGM concentrations along the cruise routes. The mean contributions over JHI, HNI, DSL, ECS, and YS are denoted by the pie charts.

The anthropogenic contributions to TGM along the cruise routes are plotted in Figure 6e, demonstrating significantly higher values near the coastal zones compared to the open ocean areas. In details, anthropogenic contributions to TGM near the East China Sea coastal zones reached as high as 60-88%, while the contributions diminished quickly to 15-25% over the open oceans. From

the northern oceanic regions to the southern counterparts, the contribution of anthropogenic sources to TGM generally exhibited a decreasing trend, with values of around 59%, 3840%, 3536%, and 296% over JHI, YS, HNI, and ECS, respectively. In comparison, previous isotope-based source apportionment studies have revealed anthropogenic contributions of 29% and 42% to TGM in remote areas like Changbai Mountain and Ailao Mountain (Wu et al., 2023). In general, the isotopebased results indicated that the relative contributions of anthropogenic emissions to surface GEM in remote China and urban China were around 30% and 49%, respectively (Fu et al., 2021; Feng et al., 2022; Wu et al., 2023). Notably, the anthropogenic contributions to TGM in the Yellow Sea, East China Sea, and Huaniao Island from this study aligned closely with isotope-derived values from China's remote regions, while the DSL findings corresponded with urban isotope results. The elevated contribution observed at JHI (59%) may be attributed to its proximity to the mainland (only 10 km away) and the sampling period occurring during the winter heating season, where continental transport influences were significant (Li et al., 2023). Furthermore, the values obtained in this study fell within comparable ranges to modeling study estimates (typically 33% to 41% on average) (Chen et al., 2014; Wang et al., 2018). As shown in Figure S1, the backward trajectories over the Yellow Sea segment were primarily influenced by air masses from the North China Plain and Liaoning Province. The relatively higher contribution of anthropogenic sources to the Yellow Sea during the cruise was likely attributable to the continental transport from northern China. The main eause of this phenomenon was that the Yellow Sea is a more enclosed maritime area compared to the East China Sea, making it more susceptible to terrestrial transport influences. In addition, during this cruise, the seawater temperature of the Yellow Sea was significantly lower than that of the East China Sea, which was unfavorable for the natural release of mercury.

522

523

524

525

526

527

528

529

530 531

532

533

534

535

536

537 538

539

540

541

542

543

544 545

546

547

548

549

550

3.4 Effects of anthropogenic inputs on the sea-air exchange of mercury

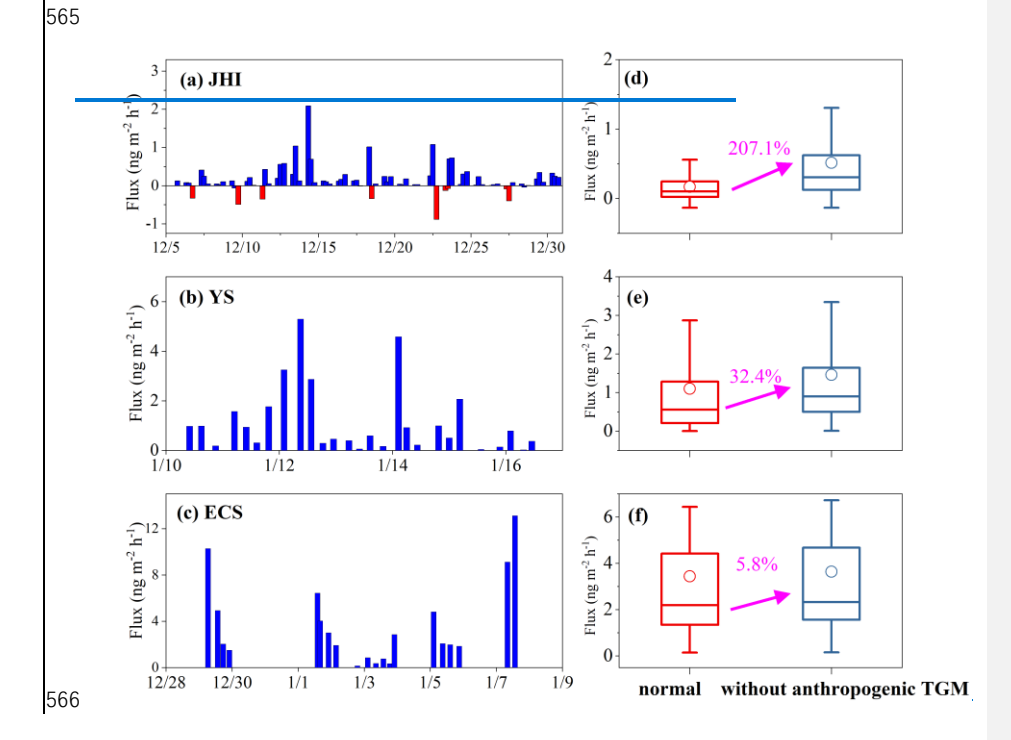
To determine the sea-air exchange flux of mercury, DGM (dissolved gaseous mercury) concentrations in seawater were measured at all sampling sites during the cruise (Figure S6). Figure S6 delineates the time-series of DGM observed at JHI, YS, HNI, and ECS, with mean concentrations of 21.3 ± 4.8 , 29.9 ± 6.1 , 42.0 ± 9.4 , and 39.7 ± 10.9 pg/L, respectively. The DGM concentrations measured during this winter cruise campaign (22.9-39.7 pg/L) were significantly lower than those

Field Code Changed

Field Code Changed

Field Code Changed

recorded previously during summer and fall in similar regions (52.4-63.9 pg/L) The DGM concentrations measured during this winter cruise campaign were significantly lower than those recorded previously during summer and fall in similar regions (Ci et al., 2011; Ci et al., 2015; Wang et al., 2016a), indicating a noticeable seasonal variation in DGM concentrations in the ECS and YS. Spatially, DGM concentrations in the ECS were higher than those in the YS, likely due to the significantly higher sea surface temperature in the ECS (mean: 14.8 °C) compared to the YS (mean: 4.1 °C) during the cruise campaign. Higher temperatures not only favored the production of DGM in seawater (Costa and Liss, 1999; Andersson et al., 2011; Mason et al., 2001), but also promoted the escape of DGM from the water surface into the atmosphere (Osterwalder et al., 2021; Huang and Zhang, 2021). Higher temperature was generally more favorable for the formation of DGM. Additionally, we observed that DGM concentrations were higher in coastal waters, particularly near the Yangtze River Estuary, where the concentration reached 51.4 pg/m³. This suggested that continental inputs, such as river discharge, had a significant influence on DGM levels in nearshore waters (Chen et al., 2020; Kuss et al., 2018; Liu et al., 2016).



Field Code Changed

Formatted: Font: 10.5 pt, Not Italic
Formatted: Font: 10.5 pt
Formatted: Font: 10.5 pt, Not Italic
Formatted: Font: 10.5 pt
Formatted: Font: 10.5 pt, Not Italic

Formatted: Font: 10.5 pt Formatted: Font: 10.5 pt

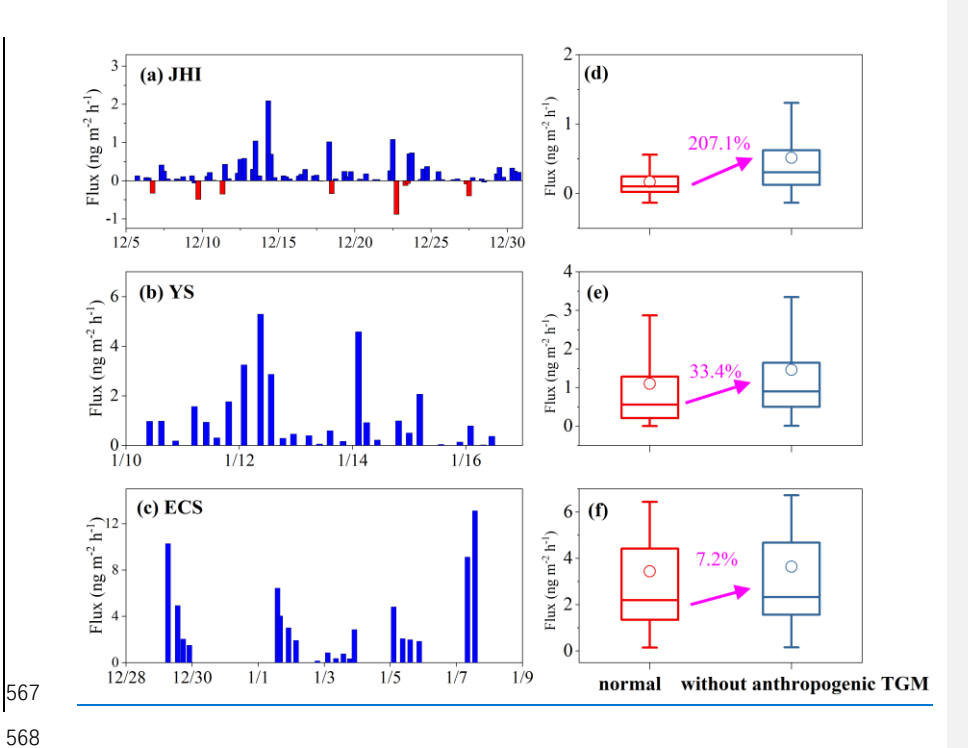


Figure 7. (a-c) Sea-air exchange fluxes of mercury at JHI, YS, and ECS, respectively. (d-f) Comparison between the normal condition and the "without anthropogenic TGM" scenario, which represented recalculated sea-air exchange fluxes of mercury after subtracting the anthropogenic contributions of TGM concentrations.

Figure 7 shows the sea-air exchange fluxes of mercury within the BS (represented by JHI), YS, and ECS, which were 0.17 ± 0.38 , 1.10 ± 1.34 , and 3.44 ± 3.24 ng m⁻² h⁻¹, respectively (Table S1). It was evident that the Hg⁰ fluxes during winter in the ECS was the highest, followed by the YS and the BS. BS acted as a weak mercury source region and even a mercury sink sometimes (negative flux in Figure 7a). Mercury fluxes observed during winter were lower than previous studies in other seasons, e.g., 4.6 ± 3.6 ng m⁻² h⁻¹ in ECS during summer (Wang et al., 2016a), 3.07 ± 3.03 ng m⁻² h⁻¹ in YS during spring (Wang et al., 2020), and 0.59 ± 1.13 ng m⁻² h⁻¹ in BS during fall (Wang et al., 2020). To assess the impacts of anthropogenic inputs on the sea-air exchange, we recalculated the flux after removing the anthropogenic contributions from the TGM measurements. This

Field Code Changed
Field Code Changed
Field Code Changed

recalculation revealed increases of mercury fluxes in all investigated oceanic regions with different extents. The post-adjustment mercury fluxes in the BS, YS, and ECS increased by 0.347, 0.357, and 0.199 ng m⁻² h⁻¹, respectively, corresponding to increased marine mercury emissions of 0.058, 0.308, and 0.332 tons, respectively. Compared to the normal condition, the BS exhibited the most substantial increase in marine mercury release (207.1%) following the deduction of anthropogenic impacts, succeeded by the YS (32.433.4%) and the ECS (5.86.5%) (Figure 7d-7f). These results quantitatively elucidated the impact of anthropogenic emissions on marine mercury release, underscoring the potential effects of diminished anthropogenic emissions on oceanic mercury cycling.

4. Conclusions and implications

This study elucidated the effects of anthropogenic sources on atmospheric mercury concentrations across various marginal seas and the subsequent influence on sea-air exchange dynamics of mercury. Through comprehensive observations across island, cruise, and terrestrial settings, we delineated atmospheric mercury distribution characteristics within the Chinese marginal seas. The relationships between TGM and various environmental parameters suggested the significance of natural sources in constraining oceanic atmospheric mercury levels. Notably, TGM peaks recorded at terrestrial and island sites exemplified the influence of continental outflows on the marine TGM. The introduction of the TGM/BC ratio functioned as a qualitative proxy for assessing the extent of anthropogenic contributions. Furthermore, we articulated a quantitative methodology for assessing anthropogenic contributions to marine atmospheric mercury, revealing that these sources contributed 59%, 3840%, and 2629% to atmospheric mercury levels across the Bohai Sea, Yellow Sea, and East China Sea, respectively. The winter sea-air exchange fluxes of mercury in these three seas were estimated as 0.169, 1.100, and 3.442 ng m⁻² h⁻¹, respectively, with increases of 0.347, 0.357, and 0.199 ng m⁻² h⁻¹ subsequent to deducting anthropogenic contributions.

Conducting atmospheric mercury measurements over oceans presented considerable complexities compared to terrestrial observations, further compounded by challenges associated with determining atmospheric mercury sources in the oceanic environment. This study established a quantitative method grounded in extensive observations encompassing terrestrial, island, and

Formatted: Font: 10.5 pt

marine contexts, facilitating estimations of anthropogenic contributions to atmospheric mercury solely predicated on atmospheric mercury and black carbon data. This methodology may offer valuable insights for analogous analyses of atmospheric mercury and other pollutants across diverse oceanic regions globally. Using this method, we further quantified the extent to which anthropogenic sources suppressed the sea-air exchange of mercury. Against the backdrop of declining global anthropogenic atmospheric mercury emissions over the past 30 years, our findings suggested an increase in mercury release from the ocean. Consequently, the mercury content in the ocean will be likely to decrease, resulting in less inorganic mercury available for methylmercury production. These insights contribute to a deeper understanding of the biogeochemical cycle of mercury and enhance our ability to evaluate its impacts on marine ecosystems and human health.

Data Availability Statement

The raw data generated in this study have been uploaded to Zenodo

(https://doi.org/10.5281/zenodo.14847622).

Author contributions

KH designed this study. XQ, HL, JC, XW, GW, CL, DL, JH, and YL performed data collection.

XQ and KH performed data analysis and wrote the paper. All have commented on and reviewed the

630 paper.

Competing interests

The authors declare that they have no conflict of interest.

Acknowledgments

This work was financially supported by the National Key R&D Plan Programs (2023YFE0102500, 2018YFC0213105), and the National Science Foundation of China (42175119, 42361144711), and the Joint Research Fund of the "Island Atmosphere and Ecology" Category IV Peak Discipline (ZD202502). Junjie Wei, Hao Ding, and Qiongzhen Wang acknowledge financial support from Central Guiding Local Science and Technology Development Fund Projects

641 (No.2023ZY1024). 642 643 References: 644 Amyot, M., Mierle, G., Lean, D. R. S., and McQueen, D. J.: SUNLIGHT-INDUCED FORMATION OF Field Code Changed 645 DISSOLVED GASEOUS MERCURY IN LAKE WATERS, Environmental science & technology, 28, 646 2366-2371, 10.1021/es00062a022, 1994. 647 Andersson, M. E., Gårdfeldt, K., Wängberg, I., and Strömberg, D.: Determination of Henry's law 648 constant for elemental mercury, Chemosphere, 649 https://doi.org/10.1016/j.chemosphere.2008.05.067, 2008a. Field Code Changed 650 Andersson, M. E., Sommar, J., Gårdfeldt, K., and Jutterström, S.: Air-sea exchange of volatile 651 mercury in the North Atlantic Ocean. Mar. Chem.. 125. 1-7.https://doi.org/10.1016/j.marchem.2011.01.005, 2011. Field Code Changed 652 653 Andersson, M. E., Sommar, J., Gårdfeldt, K., and Lindqvist, O.: Enhanced concentrations of dissolved 654 gaseous mercury in the surface waters of the Arctic Ocean, Mar. Chem., 110, 190-194, 655 10.1016/j.marchem.2008.04.002, 2008b. 656 Bencardino, M., D'Amore, F., Angot, H., Angiuli, L., Bertrand, Y., Cairns, W., Diéguez, M. C., 657 Dommergue, A., Ebinghaus, R., Esposito, G., Komínková, K., Labuschagne, C., Mannarino, V., Martin, 658 L., Martino, M., Neves, L. M., Mashyanov, N., Magand, O., Nelson, P., Norstrom, C., Read, K., 659 Sholupov, S., Skov, H., Tassone, A., Vítková, G., Cinnirella, S., Sprovieri, F., and Pirrone, N.: Patterns 660 and trends of atmospheric mercury in the GMOS network: Insights based on a decade of 661 measurements. Environmental Pollution. 363 662 https://doi.org/10.1016/j.envpol.2024.125104, 2024. Field Code Changed 663 Briggs, N. L. and Long, C. M.: Critical review of black carbon and elemental carbon source 664 apportionment in Europe and the United States, Atmospheric Environment, 144, 409-427, 665 10.1016/j.atmosenv.2016.09.002, 2016. 666 Chen, Y.-S., Tseng, C.-M., and Reinfelder, J. R.: Spatiotemporal Variations in Dissolved Elemental 667 Mercury in the River-Dominated and Monsoon-Influenced East China Sea: Drivers, Budgets, and 668 Implications, Environmental science & technology, 54, 3988-3995, 10.1021/acs.est.9b06092, 2020. Ci, Z., Wang, C., Wang, Z., and Zhang, X.: Elemental mercury (Hg(0)) in air and surface waters of 669 670 the Yellow Sea during late spring and late fall 2012: Concentration, spatial-temporal distribution 671 and air/sea flux, Chemosphere, 119, 199-208, https://doi.org/10.1016/j.chemosphere.2014.05.064, Field Code Changed 672 673 Ci, Z. J., Zhang, X. S., Yin, Y. G., Chen, J. S., and Wang, S. W.: Mercury Redox Chemistry in Waters 674 of the Eastern Asian Seas: From Polluted Coast to Clean Open Ocean, Environmental science & 675 technology, 50, 2371-2380, 10.1021/acs.est.5b05372, 2016. 676 Ci, Z. J., Zhang, X. S., Wang, Z. W., Niu, Z. C., Diao, X. Y., and Wang, S. W.: Distribution and air-sea 677 exchange of mercury (Hg) in the Yellow Sea, Atmospheric Chemistry and Physics, 11, 2881-2892, 678 10.5194/acp-11-2881-2011, 2011. 679 Costa, M. and Liss, P. S.: Photoreduction of mercury in sea water and its possible implications for 680 Hg0 air-sea fluxes, Mar. Chem., 68, 87-95, https://doi.org/10.1016/S0304-4203(99)00067-5, 1999. Field Code Changed 681 Feinberg, A., Selin, N. E., Braban, C. F., Chang, K.-L., Custodio, D., Jaffe, D. A., Kyllonen, K., Landis,

M. S., Leeson, S. R., Luke, W., Molepo, K. M., Murovec, M., Nerentorp Mastromonaco, M. G., Aspmo

682

- 684 decreases explain recent atmospheric mercury concentration declines, Proceedings of the National
- 685 Academy of Sciences of the United States of America, 121, e2401950121,
- 686 10.1073/pnas.2401950121, 2024.
- 687 Fitzgerald, W. F., Lamborg, C. H., and Hammerschmidt, C. R.: Marine Biogeochemical Cycling of
- 688 Mercury, Chemical Reviews, 107, 641-662, 10.1021/cr050353m, 2007.
- 689 Fu, X., Yang, X., Tan, Q., Ming, L., Lin, T., Lin, C.-J., Li, X., and Feng, X.: Isotopic Composition of
- 690 Gaseous Elemental Mercury in the Marine Boundary Layer of East China Sea, Journal of
- 691 Geophysical Research: Atmospheres, 10.1029/2018jd028671, 2018.
- 692 Fu, X. W., Feng, X. B., Yin, R. S., and Zhang, H.: Diurnal variations of total mercury, reactive mercury,
- 693 and dissolved gaseous mercury concentrations and water/air mercury flux in warm and cold
- seasons from freshwaters of southwestern China, Environ. Toxicol. Chem., 32, 2256-2265,
- 695 10.1002/etc.2323, 2013.
- 696 Fu, X. W., Feng, X. B., Zhang, G., Xu, W. H., Li, X. D., Yao, H., Liang, P., Li, J., Sommar, J., Yin, R. S.,
- 697 and Liu, N.: Mercury in the marine boundary layer and seawater of the South China Sea:
- 698 Concentrations, sea/air flux, and implication for land outflow, J. Geophys. Res.-Atmos., 115, 11,
- 699 10.1029/2009jd012958, 2010.
- 700 Gardfeldt, K., Sommar, J., Ferrara, R., Ceccarini, C., Lanzillotta, E., Munthe, J., Wangberg, I., Lindqvist,
- 701 O., Pirrone, N., Sprovieri, F., Pesenti, E., and Stromberg, D.: Evasion of mercury from coastal and
- 702 open waters of the Atlantic Ocean and the Mediterranean Sea, Atmospheric Environment, 37, S73-
- 703 S84, 10.1016/s1352-2310(03)00238-3, 2003.
- Horowitz, H. M., Jacob, D. J., Zhang, Y., Dibble, T. S., Slemr, F., Amos, H. M., Schmidt, J. A., Corbitt,
- 705 E. S., Marais, E. A., and Sunderland, E. M.: A new mechanism for atmospheric mercury redox
- chemistry: implications for the global mercury budget, Atmospheric Chemistry and Physics, 17,
- 707 6353-6371, 10.5194/acp-17-6353-2017, 2017.
- 708 Huang, S. and Zhang, Y.: Interannual Variability of Air-Sea Exchange of Mercury in the Global
- 709 Ocean: The "Seesaw Effect" in the Equatorial Pacific and Contributions to the Atmosphere,
- 710 Environmental science & technology, 55, 7145-7156, 10.1021/acs.est.1c00691, 2021.
- 711 Kalinchuk, V. V., Mishukov, V. F., and Astakhov, A. S.: Arctic source for elevated atmospheric
- 712 mercury (Hg-0) in the western Bering Sea in the summer of 2013, Journal of Environmental
- 713 Sciences, 68, 114-121, 10.1016/j.jes.2016.12.022, 2018.
- 714 Kuss, J., Holzmann, J., and Ludwig, R.: An Elemental Mercury Diffusion Coefficient for Natural
- 715 Waters Determined by Molecular Dynamics Simulation, Environmental science & technology, 43,
- 716 3183-3186, 10.1021/es8034889, 2009.
- 717 Kuss, J., Krüger, S., Ruickoldt, J., and Wlost, K. P.: High-resolution measurements of elemental
- 718 mercury in surface water for an improved quantitative understanding of the Baltic Sea as a source
- of atmospheric mercury, Atmos. Chem. Phys., 18, 4361, 2018.
- 720 Lamborg, C. H., Hammerschmidt, C. R., Bowman, K. L., Swarr, G. J., Munson, K. M., Ohnemus, D. C.,
- 721 Lam, P. J., Heimburger, L. E., Rijkenberg, M. J., and Saito, M. A.: A global ocean inventory of
- 722 anthropogenic mercury based on water column measurements, Nature, 512, 65-68,
- 723 10.1038/nature13563, 2014.
- Landis, M. S. and Keeler, G. J.: Atmospheric mercury deposition to Lake Michigan during the Lake
- 725 Michigan Mass Balance Study, Environmental science & technology, 36, 4518-4524,
- 726 10.1021/es011217b, 2002.
- 727 Laurier, F. and Mason, R.: Mercury concentration and speciation in the coastal and open ocean

- 728 boundary layer, J. Geophys. Res.-Atmos., 112, 10.1029/2006jd007320, 2007.
- Lavoie, R. A., Bouffard, A., Maranger, R., and Amyot, M.: Mercury transport and human exposure
- 730 from global marine fisheries, Scientific reports, 8, 10.1038/s41598-018-24938-3, 2018.
- 731 Li, H., Huang, K., Fu, Q., Lin, Y., Chen, J., Deng, C., Tian, X., Tang, Q., Song, Q., and Wei, Z.: Airborne
- 732 black carbon variations during the COVID-19 lockdown in the Yangtze River Delta megacities
- 733 suggest actions to curb global warming, Environ Chem Lett, 1-10, 10.1007/s10311-021-01327-3,
- 734 2021.
- 735 Li, H., Qin, X. F., Chen, J., Wang, G. C., Liu, C. F., Lu, D., Zheng, H. T., Song, X. Q., Gao, Q. Q., Xu, J.,
- 736 Zhu, Y. C., Liu, J. G., Wang, X. F., Deng, C. R., and Huang, K.: Continuous Measurement and
- 737 Molecular Compositions of Atmospheric Water-Soluble Brown Carbon in the Nearshore Marine
- 738 Boundary Layer of Northern China: Secondary Formation and Influencing Factors, J. Geophys.
- 739 Res.-Atmos., 128, 10.1029/2023jd038565, 2023.
- 740 Lin, C.-J., Gustin, M. S., Singhasuk, P., Eckley, C., and Miller, M.: Empirical Models for Estimating
- 741 Mercury Flux from Soils, Environmental science & technology, 44, 8522-8528, 10.1021/es1021735,
- 742 2010a
- 743 Lin, C. J., Pan, L., Streets, D. G., Shetty, S. K., Jang, C., Feng, X., Chu, H. W., and Ho, T. C.: Estimating
- 744 mercury emission outflow from East Asia using CMAQ-Hg, Atmos. Chem. Phys., 10, 1853-1864,
- 745 10.5194/acp-10-1853-2010, 2010b.
- 746 Lindberg, S. E., Hanson, P. J., Meyers, T. P., and Kim, K. H.: Air/surface exchange of mercury vapor
- 747 over forests The need for a reassessment of continental biogenic emissions, Atmospheric
- 748 Environment, 32, 895-908, 10.1016/s1352-2310(97)00173-8, 1998.
- 749 Liu, K., Wu, Q., Wang, L., Wang, S., Liu, T., Ding, D., Tang, Y., Li, G., Tian, H., Duan, L., Wang, X., Fu,
- 750 X., Feng, X., and Hao, J.: Measure-Specific Effectiveness of Air Pollution Control on China's
- 751 Atmospheric Mercury Concentration and Deposition during 2013-2017, Environmental science &
- 752 technology, 53, 8938-8946, 10.1021/acs.est.9b02428, 2019.
- T53 Liu, M., Chen, L., Wang, X., Zhang, W., Tong, Y., Ou, L., Xie, H., Shen, H., Ye, X., Deng, C., and Wang,
- 754 H.: Mercury export from mainland China to adjacent seas and its influence on the marine mercury
- 755 balance, Environ. Sci. Technol., 50, 6224, 2016.
- Luo, W., Wang, T., Jiao, W., Hu, W., Naile, J. E., Khim, J. S., Giesy, J. P., and Lu, Y.: Mercury in coastal
- 757 watersheds along the Chinese Northern Bohai and Yellow Seas, Journal of Hazardous Materials,
- 758 215-216, 199-207, https://doi.org/10.1016/j.jhazmat.2012.02.052, 2012.
- 759 Mao, H., Cheng, I., and Zhang, L.: Current understanding of the driving mechanisms for
- 760 spatiotemporal variations of atmospheric speciated mercury: a review, Atmos. Chem. Phys., 16,
- 761 12897-12924, 10.5194/acp-16-12897-2016, 2016.
- Mason, R. P.: Mercury emissions from natural processes and their importance in the global mercury
- 763 cycle, in: Mercury Fate and Transport in the Global Atmosphere: Emissions, Measurements and
- 764 Models, edited by: Mason, R., and Pirrone, N., Springer US, Boston, MA, 173-191, 10.1007/978-0-
- 765 387-93958-2_7, 2009.
- Mason, R. P., Lawson, N. M., and Sheu, G. R.: Mercury in the Atlantic Ocean: factors controlling air-
- sea exchange of mercury and its distribution in the upper waters, Deep Sea Research Part II: Topical
- 768 Studies in Oceanography, 48, 2829-2853, https://doi.org/10.1016/S0967-0645(01)00020-0, 2001.
- 769 Mason, R. P., Hammerschmidt, C. R., Lamborg, C. H., Bowman, K. L., Swarr, G. J., and Shelley, R. U.:
- 770 The air-sea exchange of mercury in the low latitude Pacific and Atlantic Oceans, Deep-Sea
- 771 Research Part I-Oceanographic Research Papers, 122, 17-28, 10.1016/j.dsr.2017.01.015, 2017.

Field Code Changed

- 772 Mason, R. P., Choi, A. L., Fitzgerald, W. F., Hammerschmidt, C. R., Lamborg, C. H., Soerensen, A. L.,
- and Sunderland, E. M.: Mercury biogeochemical cycling in the ocean and policy implications,
- 774 Environmental Research, 119, 101-117, 10.1016/j.envres.2012.03.013, 2012.
- 775 Mastromonaco, M. G. N., Gardfeldt, K., Assmann, K. M., Langer, S., Delali, T., Shlyapnikov, Y. M.,
- 776 Zivkovic, I., and Horvat, M.: Speciation of mercury in the waters of the Weddell, Amundsen and
- 777 Ross Seas (Southern Ocean), Mar. Chem., 193, 20-33, 10.1016/j.marchem.2017.03.001, 2017.
- 778 Nightingale, P. D., Malin, G., Law, C. S., Watson, A. J., Liss, P. S., Liddicoat, M. I., Boutin, J., and
- 779 Upstill-Goddard, R. C.: In situ evaluation of air-sea gas exchange parameterizations using novel
- 780 conservative and volatile tracers, 14, 373-387, https://doi.org/10.1029/1999GB900091, 2000.
- 781 O'Driscoll, N. J., Beauchamp, S., Siciliano, S. D., Rencz, A. N., and Lean, D. R. S.: Continuous Analysis
- 782 of Dissolved Gaseous Mercury (DGM) and Mercury Flux in Two Freshwater Lakes in Kejimkujik Park,
- 783 Nova Scotia: Evaluating Mercury Flux Models with Quantitative Data, Environmental science &
- 784 technology, 37, 2226-2235, 10.1021/es025944y, 2003.
- 785 Obrist, D., Kirk, J. L., Zhang, L., Sunderland, E. M., Jiskra, M., and Selin, N. E.: A review of global
- 786 environmental mercury processes in response to human and natural perturbations: Changes of
- 787 emissions, climate, and land use, Ambio, 47, 116-140, 10.1007/s13280-017-1004-9, 2018.
- 788 Osterwalder, S., Nerentorp, M., Zhu, W., Jiskra, M., Nilsson, E., Nilsson, M. B., Rutgersson, A.,
- 789 Soerensen, A. L., Sommar, J., Wallin, M. B., Wängberg, I., and Bishop, K.: Critical Observations of
- 790 Gaseous Elemental Mercury Air-Sea Exchange, Global Biogeochemical Cycles, 35,
- 791 10.1029/2020gb006742, 2021.
- Outridge, P. M., Mason, R. P., Wang, F., Guerrero, S., and Heimbürger-Boavida, L. E.: Updated
- 793 Global and Oceanic Mercury Budgets for the United Nations Global Mercury Assessment 2018,
- 794 Environmental science & technology, 52, 11466-11477, 10.1021/acs.est.8b01246, 2018.
- 795 Paatero, P. and Tapper, U.: POSITIVE MATRIX FACTORIZATION A NONNEGATIVE FACTOR
- 796 MODEL WITH OPTIMAL UTILIZATION OF ERROR-ESTIMATES OF DATA VALUES, Environmetrics,
- 797 5, 111-126, 10.1002/env.3170050203, 1994.
- Pacyna, E. G., Pacyna, J. M., Steenhuisen, F., and Wilson, S.: Global anthropogenic mercury emission
- 799 inventory for 2000, Atmospheric Environment, 40, 4048-4063, 10.1016/j.atmosenv.2006.03.041,
- 800 2006.
- 801 Pacyna, E. G., Pacyna, J. M., Sundseth, K., Munthe, J., Kindbom, K., Wilson, S., Steenhuisen, F., and
- 802 Maxson, P.: Global emission of mercury to the atmosphere from anthropogenic sources in 2005
- 803 and projections to 2020, Atmospheric Environment, 44, 2487-2499,
- 804 10.1016/j.atmosenv.2009.06.009, 2010.
- 805 Pacyna, J. M., Travnikov, O., De Simone, F., Hedgecock, I. M., Sundseth, K., Pacyna, E. G.,
- 806 Steenhuisen, F., Pirrone, N., Munthe, J., and Kindbom, K.: Current and future levels of mercury
- 807 atmospheric pollution on a global scale, Atmos. Chem. Phys., 16, 12495-12511, 10.5194/acp-16-
- 808 12495-2016, 2016.
- Pannu, R., Siciliano, S. D., and O'Driscoll, N. J.: Quantifying the effects of soil temperature, moisture
- 810 and sterilization on elemental mercury formation in boreal soils, Environmental Pollution, 193,
- 811 138-146, 10.1016/j.envpol.2014.06.023, 2014.
- 812 Pirrone, N., Cinnirella, S., Feng, X., Finkelman, R. B., Friedli, H. R., Leaner, J., Mason, R., Mukherjee,
- 813 A. B., Stracher, G. B., Streets, D. G., and Telmer, K.: Global mercury emissions to the atmosphere
- from anthropogenic and natural sources, Atmos. Chem. Phys., 10, 5951-5964, 10.5194/acp-10-
- 815 5951-2010, 2010.

- 816 Poissant, L., Amyot, M., Pilote, M., and Lean, D.: Mercury Water-Air Exchange over the Upper St.
- 817 Lawrence River and Lake Ontario, Environmental science & technology, 34, 3069-3078,
- 818 10.1021/es990719a, 2000.
- 819 Qin, X., Wang, F., Deng, C., Wang, F., and Yu, G.: Seasonal variation of atmospheric particulate
- 820 mercury over the East China Sea, an outflow region of anthropogenic pollutants to the open Pacific
- 821 Ocean, Atmos. Pollut. Res., 7, 876-883, 10.1016/j.apr.2016.05.004, 2016.
- 822 Qin, X., Wang, X., Shi, Y., Yu, G., Zhao, N., Lin, Y., Fu, Q., Wang, D., Xie, Z., Deng, C., and Huang, K.:
- 823 Characteristics of atmospheric mercury in a suburban area of east China: sources, formation
- 824 mechanisms, and regional transport, Atmos. Chem. Phys., 19, 5923-5940, 10.5194/acp-19-5923-
- 825 2019, 2019.
- 826 Qin, X., Zhang, L., Wang, G., Wang, X., Fu, Q., Xu, J., Li, H., Chen, J., Zhao, Q., Lin, Y., Huo, J., Wang,
- 827 F., Huang, K., and Deng, C.: Assessing contributions of natural surface and anthropogenic
- 828 emissions to atmospheric mercury in a fast-developing region of eastern China from 2015 to 2018,
- 829 Atmos. Chem. Phys., 20, 10985-10996, 10.5194/acp-20-10985-2020, 2020.
- 830 Selin, N. E.: Global Biogeochemical Cycling of Mercury: A Review, Annu. Rev. Environ. Resour., 34,
- 831 43-63, 10.1146/annurev.environ.051308.084314, 2009.
- 832 Soerensen, A. L., Mason, R. P., Balcom, P. H., and Sunderland, E. M.: Drivers of Surface Ocean
- 833 Mercury Concentrations and Air-Sea Exchange in the West Atlantic Ocean, Environmental science
- 834 & technology, 47, 7757-7765, 10.1021/es401354q, 2013.
- Soerensen, A. L., Skov, H., Jacob, D. J., Soerensen, B. T., and Johnson, M. S.: Global Concentrations
- 836 of Gaseous Elemental Mercury and Reactive Gaseous Mercury in the Marine Boundary Layer,
- 837 Environmental science & technology, 44, 7425-7430, 10.1021/es903839n, 2010a.
- 838 Soerensen, A. L., Mason, R. P., Balcom, P. H., Jacob, D. J., Zhang, Y. X., Kuss, J., and Sunderland, E.
- 839 M.: Elemental Mercury Concentrations and Fluxes in the Tropical Atmosphere and Ocean,
- 840 Environmental science & technology, 48, 11312-11319, 10.1021/es503109p, 2014.
- 841 Soerensen, A. L., Sunderland, E. M., Holmes, C. D., Jacob, D. J., Yantosca, R. M., Skov, H., Christensen,
- 842 J. H., Strode, S. A., and Mason, R. P.: An Improved Global Model for Air-Sea Exchange of Mercury:
- High Concentrations over the North Atlantic, Environmental science & technology, 44, 8574-8580,
- 844 10.1021/es102032g, 2010b.
- 845 Sprovieri, F., Pirrone, N., Bencardino, M., D'Amore, F., Carbone, F., Cinnirella, S., Mannarino, V.,
- 846 Landis, M., Ebinghaus, R., Weigelt, A., Brunke, E. G., Labuschagne, C., Martin, L., Munthe, J.,
- Wangberg, I., Artaxo, P., Morais, F., de Melo Jorge Barbosa, H., Brito, J., Cairns, W., Barbante, C.,
- Del Carmen Dieguez, M., Garcia, P. E., Dommergue, A., Angot, H., Magand, O., Skov, H., Horvat,
- M., Kotnik, J., Read, K. A., Neves, L. M., Gawlik, B. M., Sena, F., Mashyanov, N., Obolkin, V., Wip, D.,
- 850 Feng, X. B., Zhang, H., Fu, X., Ramachandran, R., Cossa, D., Knoery, J., Marusczak, N., Nerentorp,
- 851 M., and Norstrom, C.: Atmospheric mercury concentrations observed at ground-based monitoring
- sites globally distributed in the framework of the GMOS network, Atmos Chem Phys, 16, 11915-
- 853 11935, 10.5194/acp-16-11915-2016, 2016.
- 854 Streets, D. G., Devane, M. K., Lu, Z. F., Bond, T. C., Sunderland, E. M., and Jacob, D. J.: All-Time
- 855 Releases of Mercury to the Atmosphere from Human Activities, Environmental science &
- 856 technology, 45, 10485-10491, 10.1021/es202765m, 2011.
- Viana, M., Amato, F., Alastuey, A., Querol, X., Moreno, T., García Dos Santos, S., Herce, M. D., and
- 858 Fernández-Patier, R.: Chemical Tracers of Particulate Emissions from Commercial Shipping,

- 859 Environmental science & technology, 43, 7472-7477, 10.1021/es901558t, 2009.
- 860 Wang, C., Wang, Z., and Zhang, X.: Characteristics of mercury speciation in seawater and emission
- 861 flux of gaseous mercury in the Bohai Sea and Yellow Sea, Environ Res, 182, 109092,
- 862 10.1016/j.envres.2019.109092, 2020.
- 863 Wang, C., Ci, Z., Wang, Z., and Zhang, X.: Air-sea exchange of gaseous mercury in the East China
- 864 Sea, Environ Pollut, 212, 535-543, 10.1016/j.envpol.2016.03.016, 2016a.
- 865 Wang, C., Wang, Z., Hui, F., and Zhang, X.: Speciated atmospheric mercury and sea-air exchange
- 866 of gaseous mercury in the South China Sea, Atmospheric Chemistry and Physics, 19, 10111-10127,
- 867 10.5194/acp-19-10111-2019, 2019a.
- 868 Wang, C., Wang, Z., Hui, F., and Zhang, X.: Speciated atmospheric mercury and sea-air exchange
- of gaseous mercury in the South China Sea, Atmospheric Chemistry and Physics, 19, 10111-10127,
- 870 10.5194/acp-19-10111-2019, 2019b.
- 871 Wang, C., Wang, Z., Ci, Z., Zhang, X., and Tang, X.: Spatial-temporal distributions of gaseous
- 872 element mercury and particulate mercury in the Asian marine boundary layer, Atmospheric
- 873 Environment, 126, 107-116, 10.1016/j.atmosenv.2015.11.036, 2016b.
- 874 Wang, G. C., Chen, J., Xu, J., Yun, L., Zhang, M. D., Li, H., Qin, X. F., Deng, C. R., Zheng, H. T., Gui, H.
- 875 Q., Liu, J. G., and Huang, K.: Atmospheric Processing at the Sea-Land Interface Over the South
- 876 China Sea: Secondary Aerosol Formation, Aerosol Acidity, and Role of Sea Salts, J. Geophys. Res.-
- 877 Atmos., 127, 10.1029/2021jd036255, 2022.
- 878 Wang, X., Lin, C. J., and Feng, X.: Sensitivity analysis of an updated bidirectional air-surface
- exchange model for elemental mercury vapor, Atmospheric Chemistry and Physics, 14, 6273-6287,
- 880 10.5194/acp-14-6273-2014, 2014.
- Wangberg, I., Schmolke, S., Schager, P., Munthe, J., Ebinghaus, R., and Iverfeldt, A.: Estimates of
- 882 air-sea exchange of mercury in the Baltic Sea, Atmospheric Environment, 35, 5477-5484,
- 883 10.1016/s1352-2310(01)00246-1, 2001.
- Wanninkhof and Oceans, R. J. J. o. G. R.: Relationship between wind speed and gas exchange over
- 885 the ocean, 97, 7373, 1992.
- 886 Wanninkhof, R.: Relationship between wind speed and gas exchange over the ocean revisited,
- 887 Limnology and Oceanography-Methods, 12, 351-362, 10.4319/lom.2014.12.351, 2014.
- 888 Zhang, L., Wang, S., Wang, L., Wu, Y., Duan, L., Wu, Q., Wang, F., Yang, M., Yang, H., Hao, J., and
- 889 Liu, X.: Updated emission inventories for speciated atmospheric mercury from anthropogenic
- $890 \qquad \text{sources in China, Environmental science \& technology, } 49, 3185-3194, 10.1021/\text{es}504840\text{m}, 2015.$
- Zhang, Y., Jacob, D. J., Horowitz, H. M., Chen, L., Amos, H. M., Krabbenhoft, D. P., Slemr, F., St Louis,
- 892 V. L., and Sunderland, E. M.: Observed decrease in atmospheric mercury explained by global
- 893 decline in anthropogenic emissions, Proc Natl Acad Sci U S A, 113, 526-531,
- 894 10.1073/pnas.1516312113, 2016.

- 895 Zhu, W., Lin, C. J., Wang, X., Sommar, J., Fu, X., and Feng, X.: Global observations and modeling of
- 896 atmosphere-surface exchange of elemental mercury: a critical review, Atmos. Chem. Phys., 16,
- 897 4451-4480, 10.5194/acp-16-4451-2016, 2016.